Topological Elasticity of Flexible Structures

Adrien Saremi and Zeb Rocklin*

School of Physics, Georgia Institute of Technology, Atlanta, Georgia 30332-0430, USA

(Received 27 August 2019; revised manuscript received 6 December 2019; accepted 7 January 2020; published 2 March 2020)

Flexible mechanical metamaterials possess repeating structural motifs that imbue them with novel, exciting properties including programmability, anomalous elastic moduli, and nonlinear and robust response. We address such structures via micromorphic continuum elasticity, which allows highly nonuniform deformations (missed in conventional elasticity) within unit cells that nevertheless vary smoothly between cells. We show that the bulk microstructure gives rise to boundary elastic terms. Discrete lattice theories have shown that critically coordinated structures possess a topological invariant that determines the placement of low-energy modes on edges of such a system. We show that in continuum systems, a new topological invariant emerges, which relates the difference in the number of such modes between two opposing edges. Guided by the continuum limit of the lattice structures, we identify macroscopic experimental observables for these topological properties that may be observed independently on a new length scale above that of the microstructure.

DOI: 10.1103/PhysRevX.10.011052 Subject Areas: Metamaterials, Soft Matter

I. INTRODUCTION

Mechanical metamaterials, defined as structures such as origami sheets or spring networks with repeating patterns of elements, possess properties not found in uniform slabs of material, such as superior strength-to-mass ratios and vanishing (pentamode) [1–3] or even negative (auxetic) [4–7] elastic moduli or Poisson ratios. Of particular interest are flexible mechanical metamaterials, which possess low-energy deformation modes that can be used to achieve shape-changing, programmed response, and strong nonlinearities [8]. Some of these properties are now being demonstrated at microscopic length scales, via kirigami (cut) graphene ribbons [9], self-assembled patchy colloids [10], nanolithography [11], and DNA "origami" [12,13]. These cutting-edge techniques raise the question of what happens when such systems are manipulated on scales much larger than the unit cell. This case is precisely the limit of conventional solid mechanics, which occurs well above atomic scales. However, conventional elastic theory assumes a smoothly varying strain field, so it cannot capture short-distance flexible rearrangements. This result is reflected in the physics of disordered structures such as jammed packings [14,15], rigidity percolation networks [16], and fibrous materials [17], which see the emergence of new macroscopic length scales at a critical coordination number.

To address the implications of short-distance flexible rearrangements in otherwise uniform structures, we develop a novel micromorphic continuum elastic theory. While conventional Cauchy elasticity depends only on the strain of an infinitesimal region, micromorphic elasticity considers regions with additional relevant structure [18]. While this is unnecessary for conventional atomic solids, it can lead to much richer mechanical response, somewhat as liquid-crystalline order modifies conventional fluid dynamics. We consider two situations in which such a theory arises: as the long-wavelength limit of microscopic lattice theories, and as an intrinsically continuum theory based solely on macroscopic observables without recourse to a particular microstructure. In either case, the repeating spatial structure gives rise to an energetic term based on the gradient of the elastic strain, which can be integrated to yield a surface term in the elastic energy.

Our particular focus is on topologically protected boundary modes in the mechanical continuum. While topological modes typically occur in crystalline structures (with or without particular crystallographic point groups), recent work has demonstrated topological protection in quasicrystals [19,20] even in amorphous structures [21] and in nonorientable ribbons [22].

In the lattice theory, it has been shown that a topological invariant derived from the bulk structure controls the number of zero-energy modes on a given surface of mechanically critical lattices (having equal numbers of degrees of freedom (d.o.f.) and constraints, also called "Maxwell" or "isostatic") and is determined by an integer-valued topological invariant

*Corresponding author.
zebrocklin@gatech.edu

derived from the bulk structure [23,24] and leading to a wide variety of physical implications [25–29]. This result is derived from an integral around the topologically nontrivial Brillouin zone, which is not present in the continuum limit. Instead, we present an analysis resulting in a new invariant, which instead measures the *difference* between the numbers of zero modes on two opposing edges, analogous to the system's polarization rather than its surface charges. Because these systems are only marginally mechanically stable, it becomes important to consider how mechanical constraints generate energy costs based not only on strain but also on strain gradients, and these latter terms break spatial inversion symmetry, which is necessary for the type of polarization we consider. Our work reveals how marginal stability and microscopic spatial patterning give rise in continuum systems very generally to topologically protected deformation modes, raising the possibility of realizing this result in engineered systems or even observing it in biological ones.

The remainder of the paper is organized as follows. In Sec. II, we show how a model class of microstructures generates mechanical constraints that couple both to macroscopic strains and to microscopic d.o.f. In Sec. III, we show how this generates surface terms complementing bulk ones. In Sec. IV, we illustrate the general physics via a one-dimensional example. In Sec. V, we show how a simple linear-algebraic procedure based on the self-stresses (stressed states of equilibrium) captures the equilibration of the system and generates an effective theory in terms of smooth strain fields only. In Sec. VI, we introduce the topological invariant and relate it to the surface modes, relying on the continuum theory rather than a particular microstructure. In Sec. VII, we characterize the length and energy scales associated with the boundary modes and show how they can be experimentally observed. We conclude in Sec. VIII.

II. EFFECTS OF SMOOTH STRAIN FIELD ON MICROSTRUCTURE

Here, we introduce the class of mechanical systems whose energy is stored in discrete, springlike bonds and consider how these couple to external strain fields. Let $\mathbf{u}(\mathbf{r})$ denote the displacements that sites undergo at position $\mathbf{r}$ in the undeformed reference space. Consider a particular spring in a periodic crystal cell structure, and let $\mathbf{r}$ be the position of its cell, $\mathbf{p}$ the position of the center of the bond relative to the cell, and $\mathbf{b}$ the vector from one end of the bond to the other, as shown in Fig. 1. The extension of the spring is, for sufficiently smooth displacement fields (repeated *lower* indices implying summation):

$$e = \frac{1}{|\mathbf{b}|}\mathbf{b}\cdot[\mathbf{u}(\mathbf{r}+\mathbf{p}+\mathbf{b}/2)-\mathbf{u}(\mathbf{r}+\mathbf{p}-\mathbf{b}/2)], \quad (1a)$$

$$\approx \frac{b_i b_j}{|\mathbf{b}|}[1+p_k\partial_k]\partial_i u_j, \quad (1b)$$

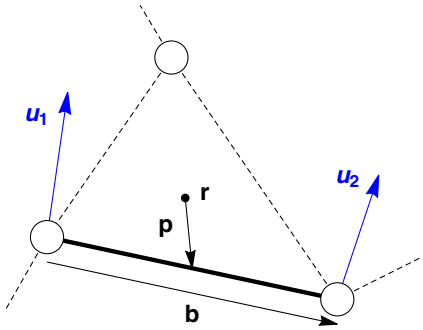

FIG. 1. A periodic spring network has a periodic microstructure consisting of bonds connecting sites, as in the generalized kagome lattice shown here. A solid bond is located at $\mathbf{p}$ relative to the center $\mathbf{r}$ of the cell in which it lies. The bond connects two sites with relative position $\mathbf{b}$, undergoing displacements $\mathbf{u}_1(\mathbf{r}), \mathbf{u}_2(\mathbf{r})$ that cause extension or compression of the bond. For continuum fields, the displacements may differ greatly for each site within the repeating cell but vary smoothly across the cells.

$$= \frac{b_i b_j}{|\mathbf{b}|}[1+p_k\partial_k]\epsilon_{ij}. \quad (1c)$$

In the preceding lines, we conduct an expansion that assumes that the displacement field is varying smoothly over the length scale of a bond, such that the relative displacements of the ends of the bond remain small. We retain a gradient in strain that will play a crucial role in distinguishing between zero- and finite-energy modes, but the smoothness of the fields ensures that the omitted higher gradients are smaller still. Because of the rotational invariance of the problem (reflected in the symmetric $b_i b_j$ prefactor), not even nonuniform rotations extend the spring, and instead we obtain a result purely in terms of the symmetrized strain $\epsilon_{ij} \equiv (1/2)(\partial_i u_j + \partial_j u_i)$ and its gradients. The strain gradient terms are usually ignored in the elasticity of rigid bodies, for which they are small for smooth strain fields. However, it is important in systems near the isostatic point, for which the contributions to the elastic energy of the conventional terms can vanish. Note also that this expression is evaluated at the position of the cell, not the bond, such that our object of interest is the strain field within the cell and the characteristics of the individual bond are encoded in $\mathbf{p}$, $\mathbf{b}$.

Notably, given that bonds repeat periodically throughout the structure, there is an ambiguity in which cell to assign which bond, the so-called discrete gauge symmetry of the lattice theory [23]. Choosing a different such assignment would shift $\mathbf{p}$ by some combination of lattice primitive vectors but would shift the point at which the strain is evaluated by an equal and opposite amount, such that the physical observable of the bond extension at a particular point in space (as opposed to a particular cell) is unchanged. Keeping this in mind, we may use the above

relationship to construct a tensor that relates the extensions $e_m(\mathbf{r})$ indexed by m to the strain field:

$$e_m(\mathbf{r}) = R^0_{m,ij}\epsilon_{ij}(\mathbf{r}), \tag{2}$$

$$R^0_{m,ij} \equiv \frac{b^m_i b^m_j}{|\mathbf{b}^m|}[1 + p^m_k \partial_k]. \tag{3}$$

Here, we introduce the initial rigidity map $\mathbf{R}^0$, which determines the spring extensions resulting from a given set of strains. Although it is the continuum analog of the rigidity (or compatibility) matrix used in lattice theories [23,30,31], we term it "initial" here because it generally results in unbalanced forces on the sites connected via the bonds, a limitation that we resolve below. Note that since this object maps from dimensionless strains to spring extensions, its elements have units of length. An alternate approach would be to calculate the fractional extensions of the springs, such that the elements of the map were rescaled by spring lengths and thus mapped from the strain of the embedding space to the strains of the springs.

III. BULK AND SURFACE ENERGIES

In the preceding section, we described a purely structural, geometrical relationship between strain fields and mechanical constraints. Here, we relate the violations of these constraints (in particular, the stretching of springs) to elastic energy. For simplicity, we consider a system with bonds of a single spring constant and choose units such that this constant (per unit volume) is unity. The resultant energy comes from the sum of the squared spring extensions, integrated across the bulk of the system:

$$E = \frac{1}{2}\int d^d\mathbf{r} e_m(\mathbf{r}) e_m(\mathbf{r}). \tag{4}$$

Given the dependence of the spring extensions on both strains and gradients [Eq. (1a)], each spring results in four energetic terms. Following a number of manipulations (see the Appendix C), the two terms that break spatial inversion symmetry may be expressed as a total divergence term and hence reduced purely to a *surface* contribution E_s to the energy expressed in terms of the outward-facing surface normal $\hat{n}$:

$$E_s = \frac{1}{2}\int_{\text{surface}} d^{d-1}\mathbf{r}\hat{n}_\alpha B^\alpha_{ijkl}\epsilon_{ij}\epsilon_{kl}, \tag{5a}$$

$$B^\alpha_{ijkl} \equiv \sum_m \frac{b^m_i b^m_j b^m_k b^m_l}{|\mathbf{b}^m|^2} p^\alpha_m. \tag{5b}$$

Therefore, these terms do not affect the bulk physics, but they do modify the response of boundaries and interfaces, analogous to total gradient terms, which are not present in nematics but do occur in cholesteric liquid crystals [32].

In addition to this surface term, we have spatial inversion symmetric terms due to the conventional strains and their gradients:

$$E_b = \frac{1}{2}\int d^d\mathbf{r} A_{ijkl}\epsilon_{ij}\epsilon_{kl} + D^{\alpha\beta}_{ijkl}(\partial_\alpha\epsilon_{ij})(\partial_\beta\epsilon_{kl}), \tag{6a}$$

$$A_{ijkl} \equiv \sum_m \frac{b^m_i b^m_j b^m_k b^m_l}{|\mathbf{b}^m|^2}, \tag{6b}$$

$$D^{\alpha\beta}_{ijkl} \equiv \sum_m \frac{b^m_i b^m_j b^m_k b^m_l}{|\mathbf{b}^m|^2} p^\alpha_m p^\beta_m. \tag{6c}$$

We recognize that the energy consists of three types of terms: conventional bulk strain energies leading to elasticities of the sort described in Ref. [30], surface strain terms, and higher-order bulk terms consisting of strain gradients. Expanding the initial rigidity map further would generate higher-order bulk and surface terms. The bulk terms are even under spatial inversion and the boundary terms are odd. Because of this, the surface energies may be either positive or negative, depending on the spatial

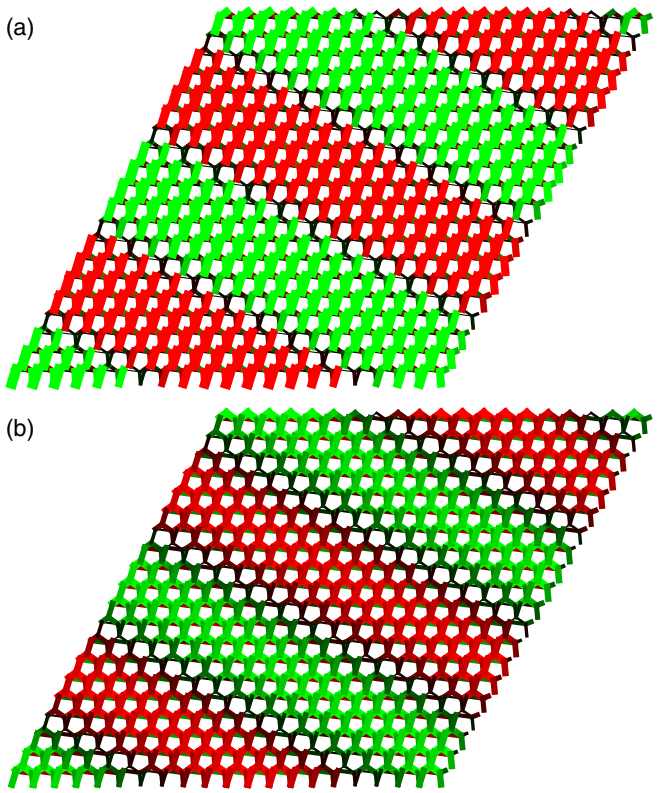

FIG. 2. (a) On a periodic system, we apply a particular strain $\epsilon_{ij}(\mathbf{r}) = (\epsilon_{xx}, \epsilon_{yy})e^{i(\mathbf{q}\cdot\mathbf{r})}$. This strain causes bonds to stretch (green) or compress (red). (b) The system then relaxes by projecting onto the space of self-stresses that mostly capture particles displacing over short distances but reducing the energy cost overall.

distribution of the strain field, hinting at how zero-energy modes may manifest in a Maxwell lattice despite their necessarily positive bulk energies.

As discussed in Ref. [33], Maxwell lattices in 2D necessarily have a Guest mode, a zero-energy linear deformation that also extends nonlinearly. The nonlinear deformation is beyond the scope of the present work, but the linear zero-energy deformation necessarily appears as a combination of strains that is a zero-energy eigenmode of the elasticity tensor. Because of this nonlinear instability, a Maxwell lattice necessarily has multiple zero-energy configurations; the bond and position vectors of the preceding equations are associated with one particular configuration. Indeed, as shown in Ref. [34], altering the configuration can change the lattice topological polarization.

Note that we have not yet made any assumptions about either mechanical equilibrium or mechanical criticality. As such, even when the conventional elastic force balance is achieved (i.e., the divergence of the stress vanishes in the bulk), there are unbalanced forces on the individual d.o.f. shown in Fig. 2(a). Before we rectify this, let us illustrate the bulk and boundary energies with a minimal example, occurring in one dimension and with a single strain component.

IV. EQUILIBRIUM IN ONE-DIMENSIONAL SYSTEMS

To illustrate the essential components of our strain gradient theory without the complications of several d.o.f. and higher dimensions, in this section, we derive a minimal gradient elastic limit of a one-dimensional discrete system analogous to the rotor chain of Ref. [23], with the additional feature of elastic systems that uniform translations do not violate constraints. The simplest linear relationship between a constraint e_n and the displacements $\{u_n\}$ is then

$$e_n = au_{n+1} - (a+b)u_n + bu_{n-1}. \tag{7}$$

A direct solution would indicate that the zero-energy modes consist of a uniform translation and an exponentially localized "strain" $u_{n+1} - u_n = (b/a)^n$. The long-wavelength limit is valid when all modes, including this one, are smooth over the length ℓ of the unit cell, requiring that $\log|b/a| \ll 1$. In this limit, we can Taylor expand the displacement as $u_{n\pm1} = u_n \pm \ell u_n' + (1/2)\ell^2 u_n''$, resulting in an energy functional

$$E = \frac{\ell}{2}\int dx[(a-b)u'(x) + \ell/2(a+b)u''(x)]^2, \tag{8a}$$

$$= \frac{k}{2}\int dx[u'(x) - \alpha u''(x)]^2, \tag{8b}$$

$$= \frac{k}{2}\left[-\alpha(u')^2|_{-d/2}^{d/2} + \int dx(u'(x)^2 + \alpha^2 u''(x)^2)\right], \tag{8c}$$

where we have defined, in terms of our microscopic parameters a, b, two macroscopic parameters: $k = \ell(a-b)^2$, which sets the energy scale, and a (signed) length scale $\alpha = (\ell/2)(a+b)/(b-a)$. This case is the linear limit of the nonlinear edge mode that was found to extend into a soliton in Ref. [35], with strain playing the role of the rotor angle. By performing a functional derivative with respect to the displacement field $u(x)$, we can obtain the conditions for force balance in the bulk, namely, that $(\alpha^2\partial^2 - 1)u''(x) = 0$, resulting in a general equilibrium profile consisting of two boundary modes, a uniform strain and a trivial translation:

$$u(x) = c_- e^{-(x+d/2)/\alpha} + c_+ e^{(x-d/2)/\alpha} + \epsilon_0 x + u_0, \tag{9}$$

where definitions are chosen such that for $\alpha > 0$ the first mode is exponentially localized to the left edge, $x = -d/2$, with an amplitude there of c_-, and the second is exponentially localized to the right edge, $x = d/2$, with an amplitude there of c_+. The energy functional of Eq. (8) may then be expressed as

$$E = \frac{k}{2}\left[\frac{2c_-^2}{\alpha}(1 - e^{-2d/\alpha}) - 4c_-\epsilon_0(1 - e^{-d/\alpha}) + d\epsilon_0^2\right], \tag{10}$$

where the terms proportionate to powers of $\exp(-d/\alpha)$ vanish in the limit of large system size (for $\alpha > 0$). Note that the energy depends only on the bulk strain ϵ_0 and the c_- mode. As can be seen by direct substitution into the energy functional, c_+ is a zero-energy mode that does not violate any of the microscopic constraints. However, $c_\pm$ appear, respectively, on the right and left sides when $\alpha > 0$ and are reversed for $\alpha < 0$. Hence, the surface term of Eq. (8c) determines that there is a zero mode (c_+), and its sign determines on which surface the mode appears. In general, though, a non-Maxwell continuum theory (such as would arise, e.g., when there were two microscopic constraints for each d.o.f.) could have a surface term but no zero modes. This case also illustrates the general principle that this surface term, and hence the zero-energy modes, cannot be derived from the bulk energetics, which are invariant under spatial inversion. Therefore, in the following sections, we return to a general form of the bulk constraints in order to consider the effects of mechanical equilibrium, mechanical criticality, and topological protection.

Given the four modes of the general form of the displacement field, Eq. (9), four boundary conditions must be specified. The natural choice is to enforce the displacement and strain on both boundaries, $u(\pm d/2) = u_\pm$, $u'(\pm d/2) = u'_\pm$. The resulting energy functional is, in the large-system-size limit,

$$E = \frac{k}{2}\left[\frac{(u_+ - u_-)^2}{d} + 2\alpha(u'_\pm)^2\right], \tag{11}$$

reflecting the bulk contribution from the average strain $(u_+ - u_-)/d$ and the local strain at whichever boundary hosts the nonzero mode (u'_- when $\alpha > 0$ and the nonzero-energy mode is on the left, u'_+ when $\alpha < 0$).

V. MECHANICAL RELAXATION AND EQUILIBRIUM IN THE MICROSTRUCTURE

From the energy functional of Eq. (4), we may obtain the stress tensor $\sigma_{ij}(\mathbf{r}) = \delta E/\delta\epsilon_{ij}(\mathbf{r})$ [36] with the details of the functional differentiation described in Appendix A. Just as each bond extension is obtained as a linear operator on the strain, now the stress is obtained as a linear operator on the bond extensions, which we denote as the initial equilibrium map $Q^0_{ij,m}$, again in analogy to the equilibrium matrix of lattice theories:

$$\sigma_{ij}(\mathbf{r}) = Q^0_{ij,m} e_m(\mathbf{r}), \tag{12}$$

$$Q^0_{ij,m} \equiv \frac{b^m_i b^m_j}{|\mathbf{b}|}[1 - p_k\partial_k]. \tag{13}$$

The above equations describe the elastic relationships between stress, strain, bond extensions, and energy. Note that these results mirror those of the lattice theories [30]. In particular, if we consider modes with spatial variation $\exp(i\mathbf{q}\cdot\mathbf{r})$, the equilibrium map is simply the transpose of the rigidity map at the opposing wave vector:

$$Q^0_{ij,m}(\mathbf{q}) = R^0_{m,ij}(-\mathbf{q}). \tag{14}$$

However, the smooth strain fields assumed here are unrealistic for isostatic systems, which undergo short-wavelength nonaffine relaxation events to dramatically lower their energy in response to unbalanced forces within the unit cell.

Consider, as we have above, the extensions of bonds that occur when a strain field is imposed externally. These extensions generate tensions, which in turn generate unbalanced forces on the sites. These forces result in additional displacements of the sites, achieving force balance and energy minimization. These displacements may of course be obtained by solving whatever microscopic force-balance equations are appropriate to a given microstructure, but a more elegant and efficient method exists for systems close to the isostatic point. For such systems, there are only a few states of self-stress [23,31], which are sets of tensions that generate no force on any site. As has been shown [24], the postrelaxation bond extensions $\mathbf{e}$ are precisely the projection of the pre-relaxation bond extensions $\mathbf{e}_0$ into the space spanned by an orthonormal set of states of self-stress, $\{\mathbf{s}_i\}$.

For Maxwell lattices, which have equal numbers of site d.o.f. and bond constraints, this technique has proven useful to obtain the uniform elastic response. Such a lattice has d modes of translation that result, via the Maxwell-Calladine index theorem, in d states of self-stress. The $d(d+1)/2$ components of the elasticity tensor are all obtained from these modes, implying that $d(d-1)/2$ strains cost zero energy. These modes are known as Guest modes [33]. This method, which naturally accounts for the large intracell relaxation, yields the correct moduli, whereas assuming a uniform strain field overestimates them substantially.

In the present analysis, we consider external fields that are applied over length scales that are large compared to the unit cell, such that displacement fields necessarily vary smoothly over these scales. At the same time, the fields may vary dramatically *within* the cell, such as when, e.g., a rigid triangular unit undergoes a rotation. To that end, we consider the behavior of structures such that the center of mass of each cell is coupled to external fields (such as those induced by smooth, rigid mechanical barriers), while the other, internal d.o.f. (rotations and shears) are allowed to relax and achieve mechanical equilibrium. In this way, we retain a theory expressing the energetics in terms of the slowly varying strain field across the periodic structure while still permitting deformations that relax energy within the crystal cell.

Thus, we identify the smooth displacement (alternately, strain) fields $\mathbf{u}(\mathbf{r}) = \mathbf{u}\exp(i\mathbf{q}\cdot\mathbf{r})$. These are the fields we wish to retain, while the short-range relaxations within the unit cell are allowed to occur to lower the system energy. Note that although $\mathbf{u}$ has only d components, it captures all of the allowed strains. For $\mathbf{q} \neq 0$, there exist $d(d-1)/2$ mechanical compatibility conditions [33] that are satisfied by the $d(d+1)/2$ components of the strain, such that they do indeed derive from a valid displacement field defined by d components.

How, then, do we allow relaxation of the remaining d.o.f.? Previously, we required that all the components of the force $\mathbf{f} = \mathbf{Q}\mathbf{e}$ on the sites resulting from the extensions must vanish. Now, though, we allow forces on the smooth strain fields to remain unbalanced. For example, if we consider a set of strain fields that generates a force on the center of mass of a cell and a torque on one of its rigid elements, we would allow the cell to relax to alleviate the torque while retaining the center-of-mass force. In other words, if $\{|v_i\rangle\}$ are the set of externally imposed center-of-mass displacements on the cells, we allow no center-of-mass forces, such that we allow $\langle v_i|f\rangle \neq 0$ but require that the other components of the forces vanish. To that end, our self-stresses are now defined as an orthonormal basis for the null space of the equilibrium matrix with these modes projected out:

$$\{|s_j\rangle\} = \mathrm{Null}(\mathbb{1} - |v_i\rangle\langle v_i|)\mathbf{Q}. \tag{15}$$

For the periodic systems currently under consideration, modes at different wave vectors are orthogonal.

Consequently, we can consider rigidity and equilibrium maps at a particular wave vector, such that $\partial_j \to iq_j$ and a strain at a given wave vector results in spring extensions only at the same wave vector. Consequently, there are only d modes at any given wave vector that need be projected out in Eq. (15). Each such mode consists of displacements of sites along one of the Cartesian directions, with spatial dependence $\exp(i\mathbf{q}\cdot\mathbf{r})$. The result is d states of self-stress.

We thus obtain the primary object under consideration in the present work, the rigidity map $R_{m,ij}$, which describes the extensions that result from a smooth strain field following the short-distance relaxations within the unit cell. From this result, the equilibrium map may be derived in precisely the same way as the initial equilibrium map was derived from the initial rigidity map. In terms of the initial rigidity map of Eq. (3) and $s_{m,n}$, the nth component of the mth state of self-stress is as follows:

$$R_{m,ij}(\mathbf{q}) = s^*_{m,n}\mathbf{R}^0_{n,ij}(\mathbf{q}), \tag{16}$$

$$Q_{ij,m}(\mathbf{q}) = \mathbf{Q}^0_{ij,n}(\mathbf{q})s_{m,n}. \tag{17}$$

The above analysis implies that, if we think of the rigidity map as a matrix acting on the d independent components of the strain, it similarly results in d independent self-stresses and is thus a square matrix. This is precisely the Maxwell condition for lattice theories: that the energetic constraints and the d.o.f. are equal in number. Thus, we arrive at a natural condition to extend the Maxwell condition to theories of continuum fields: that the configuration spaces and constraints be equal in number.

A final property proves crucial to the low-energy response of the lattice. The aforementioned Guest modes ensure that the rigidity maps have zero modes at low wave vectors. In other words, generically, the eigenvalues of the rigidity map would have $O(q^0)$ components, yet for the Guest mode the leading contribution would be $O(q^1)$.

VI. TOPOLOGICAL POLARIZATION IN THE CONTINUUM

We have now generated a continuum map that describes the relationship between local strain d.o.f. and a like number of energetic constraints, retaining the Maxwell criterion of the lattice theories. However, it is not *a priori* clear that this formulation captures the phenomena of the lattice theory, including topological protection of modes at interfaces, edges, and defects. Such modes are generated and protected by topological invariants defined by the homotopy class of loops across the Brillouin zone, which no longer exists in our continuum formulation. Do the zero modes have continuum descriptions, and do they retain topological protection? We answer these questions in the affirmative.

Since we mean to include edge modes, we allow $\mathbf{q}$ to be complex, with the imaginary part representing the rate at which the mode decays away from the edge. In particular, suppose we have an edge in the second spatial direction, on the line $(0, r_y)$, with the system extending to its right, with $r_x > 0$. A mode extending along and exponentially localized to this edge would have $\mathrm{Im}(q_y) = 0$ real and $\mathrm{Im}(q_x) > 0$, while one on the opposite edge would have $\mathrm{Im}(q_x) < 0$.

Because any extensions of bonds cost energy, zero-energy modes are precisely those that lie in the null space of the rigidity map of Eq. (16). Note that the use of this map means that we are allowing the local structure to relax to minimize energy—in this case, to zero. This linear map is a square matrix, and hence the wave vectors at which it has zero modes are precisely those at which its determinant vanishes. We thus search for the zeros of this determinant, which we write as $\det(\mathbf{R}(\mathbf{q}))$. In this way, we acquire an object dependent on wave vector only, which contains all the information about the displacement field and constraints without using their indices. Because of the two modes of translation, $\det(\mathbf{R}(\mathbf{q}))$ has a double zero at $\mathbf{q} = 0$ and hence takes the following form:

$$\mathbf{R}(\mathbf{q}) = \begin{pmatrix} R_{11}(\mathbf{q}) & R_{12}(\mathbf{q}) \\ R_{21}(\mathbf{q}) & R_{22}(\mathbf{q}) \end{pmatrix} \tag{18a}$$

$$\Rightarrow \det(\mathbf{R}(\mathbf{q})) = A_{2,0}q_x^2 + A_{1,1}q_xq_y + A_{0,2}q_y^2 + iA_{3,0}q_x^3 + iA_{2,1}q_x^2q_y + \ldots, \tag{18b}$$

with $A_{n_1n_2}$ real coefficients set by the microstructure. Because our rigidity map has units, $A_{ij}q_x^{n_1}q_y^{n_2}$ has units of the volume of d-dimensional space (two, here). Terminating the expansion to order n in q indicates the presence of n zero modes. Of these modes, two take the form

$$q_x = \alpha_\pm q_y + i\beta_\pm q_y^2, \tag{19}$$

while the others are short-wavelength modes of order q_y^0. Note that α is determined by the coefficients of order $O(q^2)$, while the signed inverse decay length $\kappa_\pm \equiv \beta_\pm q_y^2$ depends on the second and third order terms of Eq. (18b). While a lattice may have short-wavelength modes, our continuum formulation deliberately excludes them, and hence the short-wavelength modes here are nonphysical and dictated by the order at which we terminate our expansion. Our long-wavelength zero edge modes are then restricted to wave vectors obeying the above equation. The trivial state is the one in which $\kappa_\pm$ take opposing signs, whereas in a polarized state, both $\kappa_\pm$ would take the same sign. Thus, to capture the edge-mode polarization, a topological invariant must count the numbers of positive and/or negative $\kappa_\pm$.

Because the loss of periodicity destroys the Brillouin zone, a natural approach would be to perform an integral instead over all real values of q_y. This method could lead, via the extended real number line, to a noncontractible loop such as in the periodic case, analogous to an approach that was applied in Refs. [37,38] to determine Chern numbers on the surfaces of spheres rather than tori. However, this procedure would not be appropriate here since it would include the fictitious short-wavelength modes.

Instead, to capture the long-wavelength behavior, we introduce $|\mathbf{l}_1|$, the length of the first lattice primitive vector, and consider edge modes for which the transverse component of the wave vector is small: $q_y|\mathbf{l}_1| \ll 1$. In selecting modes over which to integrate, one must consider values of the remaining component of the wave vector that extend far beyond those while also ignoring fictitious short-wavelength modes. In other words, we consider values of q_x that satisfy $q_y|\mathbf{l}_1| \ll q_x|\mathbf{l}_1| \ll 1$. Then, we choose for $\epsilon \equiv q_y|\mathbf{l}_1|$ to integrate over values of $q_x|\mathbf{l}_1|$ extending to $\epsilon^{1/2}$. Per the detailed analysis and derivation in Appendix D, there are alternate methods that may capture the transition more sharply. The resulting topological invariant describing the numbers of modes on the left and right edges is

$$N_L - N_R = \frac{1}{\pi}\lim_{\epsilon\to 0^+}\int_{-\sqrt{\epsilon}/|\mathbf{l}_1|}^{\sqrt{\epsilon}/|\mathbf{l}_1|} dq_x \times \partial_{q_x}\arg\det\left(\mathbf{R}(q_x, q_y = \epsilon)\right). \quad (20)$$

Intuitively, this equation states that for topological reasons, the way in which the relationship between strains and microscopic constraints [encoded in $\det(\mathbf{R}(\mathbf{q}))$] varies with the wavelength of bulk modes is determined by the difference in the numbers of modes on the edges that satisfy these constraints. Mathematically, this relationship follows from the contour in the complex plane shown in Fig. 3. In that figure, we search for a relationship between the behavior of the bulk modes, shown on the real axis, and the zero-energy surface modes, represented as black points. Applying the argument principle means that the long-wavelength modes will cause the phase of the determinant of the rigidity map to wind by $\pm 2\pi$ for modes on the left (right) edges. However, just as the zero modes themselves, the curved portions of the contour have imaginary components of the wave vector and hence are boundary modes that cannot be considered in establishing a bulk-boundary correspondence, a key signature of topological protection. However, while the contributions of the curved portions are never small, their difference does vanish in the given limit. As such, we may determine the presence of zero modes solely through the portions of the contour corresponding to bulk modes (solid lines). In this way, the topological invariant becomes quantized (integer) precisely in the long-wavelength limit, as shown in detail in Appendix D. Indeed, this notion of the topological invariant emerging in the long-wavelength limit is implicit in other continuum treatments, insofar as they likewise consider length scales over which atomic details may be neglected. This continuum object in fact bears a closer relationship to conventional polarization than the discrete analog, which counts the number of zero modes on a particular edge rather than the difference between the two edges.

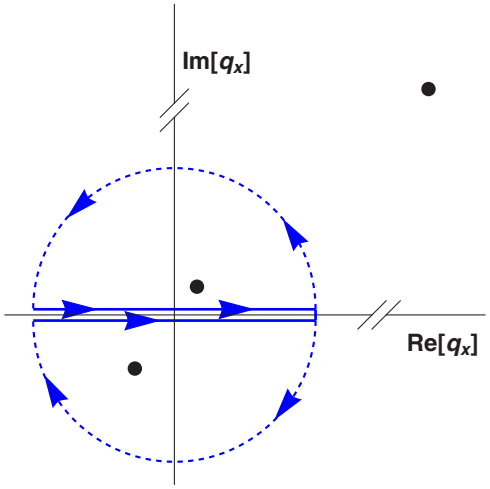

FIG. 3. The contour used to establish the relationship between the bulk structure and the locations of the zero modes. Via complex analysis, the full contour counts the difference in numbers of long-wavelength zero modes on the left and right edges while remaining insensitive to the short-wavelength modes. As described in the text, for this particular contour, the dashed portions may be neglected, such that the locations of the zero modes are determined solely by the bulk physics captured in the solid lines.

To demonstrate that nonzero topological polarizations occur, we consider a class of generalized kagome lattices, consisting of a periodic cell with three sites in two dimensions, joined by three intracellular and three intercellular bonds as shown in Fig. 4. In that figure, we consider a 1D family of such lattices that undergoes a topological transition at which deformation of the lattice shifts a boundary mode from one edge to the opposing edge, polarizing the system. As shown in Fig. 4(a), our numerical technique generates noticeable error, as described in Appendix D, very close to the transition point, which can also be identified by direct geometrical means.

A. Topological polarization as a vector

In the continuum, it becomes natural to ask about the polarization, not only at a certain interface—for now, we focus on a vertical interface, with decay along the horizontal direction (x direction)—but for every possible interface. Specifically, we look for $\Delta N(\theta_n)$—the difference between the number of zero modes on the "left" and "right" edges when the vector pointing from the left to the right

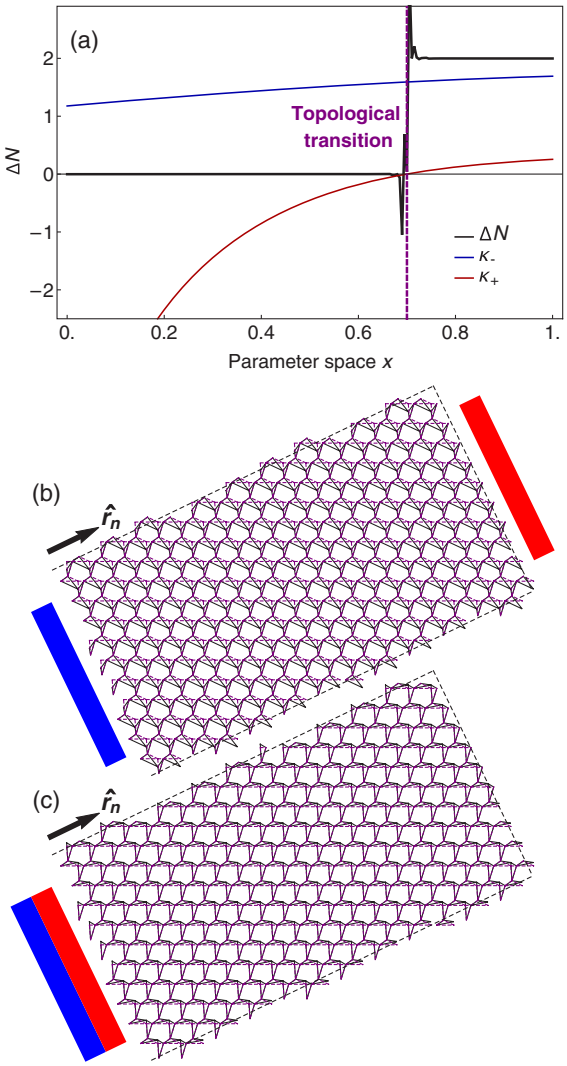

FIG. 4. (a) Topological transition as we deform the kagome lattice. The geometry of the system is parametrized as $\mathbf{g}(x) = x\mathbf{g}_1 + (1-x)\mathbf{g}_2$, where $\mathbf{g}_1$, $\mathbf{g}_2$ are geometric configurations of two kagome systems with respective topological polarizations 0 and 2 along the $\hat{r}_n$ direction. Note that $\kappa_\pm$ are the signed inverse decay lengths, such that, when one vanishes, the associated mode lies in the bulk and, when both have the same sign, the system is polarized. (b) The system in the $\mathbf{g}_1$ configuration with trivial polarization: There is a zero mode on the left side of the considered orientation $\hat{r}_n$ and one on the opposite side. (c) The system in nontrivial polarization ($\Delta N = 2$): This time, the two modes are on the left side of the direction. In all three figures, the purple dashed lines represent the shape of the system at the topological transition (when $x = 0.7$).

edge is $\hat{q}_n(\theta_n) \equiv \cos\theta_n\hat{x} + \sin\theta_n\hat{y}$. In this way, we can recast the wave vector in terms of the components along this normal direction, $q_n \equiv \hat{q}_n \cdot \mathbf{q}$, and the component q_t along the tangent direction, $\hat{q}_t(\theta_n) \equiv -\sin\theta_n\hat{x} + \cos\theta_n\hat{y}$. This method allows us to rewrite the determinant in the new (q_n, q_t) basis and find the long-wavelength modes of present interest:

$$\begin{aligned}\det(\mathbf{R}(\mathbf{q})) &= \det(q_x = \cos\theta q_n - \sin\theta q_t,\\ &\quad q_y = \sin\theta q_n + \cos\theta q_t)\\ &= A'_{2,0}q_n^2 + A'_{1,1}q_nq_t + A'_{0,2}q_t^2 + iA'_{3,0}q_n^3 + \ldots\end{aligned} \tag{21}$$

$$\Rightarrow q_n = \alpha_\pm(\theta)q_t + i\kappa_\pm(\theta)q_t^2, \tag{22}$$

where, once again, the sign of $\kappa_\pm(\theta_n) \equiv \beta(\theta_n)q_t^2$ determines the topology in a particular $\hat{r}_n(\theta_n)$ direction. This new expression allows us to describe how the topological polarization changes at different angles. What we observe is that the modes flip from one side to the other as the direction $\hat{r}_n(\theta_n)$ crosses a particular set of directions (indicated by orange lines in Fig. 5). Those regions are called soft directions, and we address their nature in the following section.

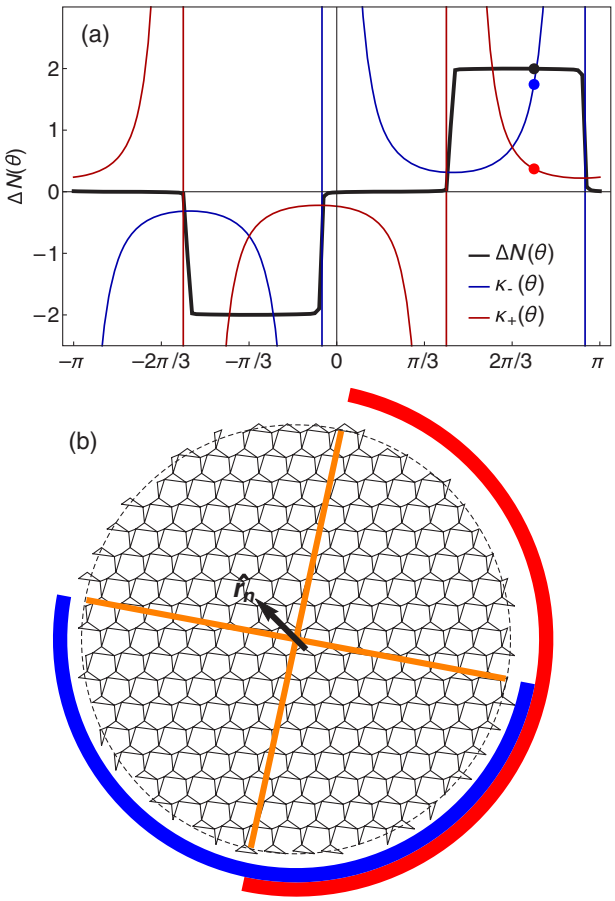

FIG. 5. (a) For a fixed system, we numerically compute the signed inverse decay lengths of each mode $[\kappa_-(\theta_n), \kappa_+(\theta_n)]$ and the topological polarization $\Delta N(\theta_n)$ as a function of the normal direction $\hat{r}_n(\theta_n)$. (b) The polarization changes as the considered direction crosses either soft direction (orange lines). One can then find the regions of the lattice where the + or − edge modes are located (blue or red arcs).

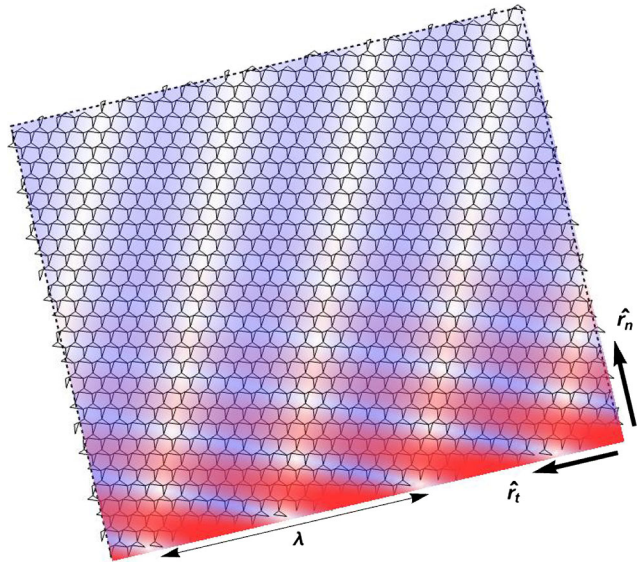

FIG. 6. Shape of the edge modes in a system with polarization $\Delta N = 2$. We impose a mode with wavelength $\lambda = 15.6|\mathbf{l}_1|$ on the boundary $\hat{r}_t$ (where $\mathbf{l}_1$ is the first lattice primitive vector). This mode then propagates through the bulk and decays along the direction $\hat{r}_n$. Each mode (red or blue) varies sinusoidally along its corresponding soft direction; therefore, it also varies along the boundary with a longer wavelength. The modes decay into the bulk over length scales much longer than this wavelength.

B. Soft directions

Focusing on the long-wavelength zero modes established in Eq. (19), we find the existence of soft directions [indicated by orange lines in Fig. 5(b)], characteristic of the lattice [39] and determined by the value of the $\alpha_\pm$ coefficients:

$$q_x = \alpha_\pm q_y \Rightarrow \hat{q}_\pm = \frac{(\alpha_\pm, 1)}{\sqrt{1+\alpha_\pm}}. \tag{23}$$

We can then rewrite the determinant of a generic wave vector $\mathbf{q}$ in this new basis, $\mathbf{q} = q_+\hat{q}_+ + q_-\hat{q}_-$:

$$\det\left(\mathbf{R}(\mathbf{q})\right) = A''_{1,1}q_+q_- + iA''_{3,0}q_+^3 + iA''_{2,1}q_+^2q_- + \ldots, \tag{24}$$

so if a wave vector lies exactly on either soft direction (i.e., $\mathbf{q} = q_+\hat{q}_+$ or $= q_-\hat{q}_-$), it is, by definition, a zero of our rigidity map, at least to second order.

VII. EXPERIMENTAL LENGTH AND ENERGY SCALES

The triumph of conventional elasticity is its ability to capture mechanical response at length scales extending to the system size, far beyond those of the underlying, unobserved atomic interactions. It is not clear *a priori* whether the boundary modes that we consider extend to macroscale systems or whether they are valid only on the "atomic" length scales of the unit cell, those already captured by the lattice theory. Indeed, the dramatic change in edge stiffness predicted by simple central-force models [34] has resulted in relatively modest differential stiffnesses in 3D-printed systems [40]. In fact, as we show here, the boundary modes extend to wavelengths that are intermediate between the unit cell and the system size, establishing new criteria for experimentally realizing strong topological effects.

Let us consider, in particular, the imposition of a distortion on a boundary with wave number q_t on an interface with tangent direction $\hat{r}_t(\theta_n)$. In order to minimize energy, the system will undergo a distortion associated with one (or both) of the two soft directions described in the preceding section. We thus search the space of zero modes described in Eq. (24) for a zero mode with the appropriate component along the surface tangent direction, resulting in a wave vector of the form

$$\mathbf{q}_\pm = \frac{q_t}{\hat{q}_\pm \cdot \hat{q}_t}\hat{q}_+ \pm iq_t^2\frac{A''_{3,0(0,3)}}{A''_{1,1}}\frac{|\hat{q}_+, \hat{q}_-|}{(\hat{q}_\pm \cdot \hat{q}_t)^3}\hat{q}_n, \tag{25}$$

where $|\hat{q}_+, \hat{q}_-|$ denotes the determinant of the matrix of the given columns. Expressed in terms of the angles $\theta_\pm$, θ_n of the soft directions and the normal direction, we get

$$\mathbf{q}_\pm = \frac{q_t}{\sin(\theta_\pm - \theta_n)}\hat{q}_\pm \pm iq_t^2\frac{A''_{3,0(0,3)}}{A''_{1,1}}\frac{\sin(\theta_+ - \theta_-)}{\sin^3(\theta_n - \theta_\pm)}\hat{q}_n. \tag{26}$$

We note that the decay part of this expression includes parameters of the systems that come from the determinant of our rigidity mapping—i.e., the A'' terms of Eq. (26)—and hence cannot be measured by the bulk response.

We now express this relationship in terms of unitless ratios (in brackets) between the quantities with units of the lattice length scale, the decay length, and the wavelength of the surface distortion, $\lambda = 2\pi/q_t$:

$$\left[\frac{\zeta_\pm}{|\mathbf{l}_1|}\right] = \pm\frac{1}{(2\pi)^2}\left[\frac{\lambda}{|\mathbf{l}_1|}\right]^2\left[\frac{|\mathbf{l}_1|A''_{1,1}}{A''_{3,0(0,3)}}\right]\frac{\sin^3(\theta_n - \theta_\pm)}{\sin(\theta_+ - \theta_-)}. \tag{27}$$

From the above expression, we see that the number of cells over which the topological mode decays is generically on the order of the square of the number of cells over which it extends on the surface, as shown in Fig. 6. For example, if the wavelength extends over thousands of unit cells, the boundary mode generically decays on the scale of millions of cells. Hence, the surface theory extends from microscopic wavelengths up to the order of the geometric mean of the system size and unit cell size. However, this geometric relationship is strongly modified by the direction of the interface. When the soft direction is nearly aligned

with the normal direction, the wavelength of the modes in the bulk becomes much smaller than that on the boundary, and the decay length is correspondingly reduced, meaning that the effect may be observed in smaller systems.

Beyond these concerns regarding the length scale, the surface theory also relies on appropriate energy scales. While a full energetic analysis is beyond the scope of the present work, consideration of microscopic interactions and length scales permits us to estimate additional criteria to observe continuum topological polarization. Real systems contain additional constraints beyond those included in the Maxwell rigidity map. In a 3D-printed frame, in addition to strong energetic costs to central-force compressions and extensions, beams possess finite bending stiffness not found in central-force springs. In our topological modes, these bending costs are imposed on a length scale proportional to the square of the wavelength, whereas a conventional Rayleigh-type surface mode would impose greater central-force energy costs over a smaller volume, extending to a depth proportional only to wavelength. Hence, the topological surface modes should only be strictly observable on wavelengths sufficiently short that they lie below the conventional modes in energy.

Finally, we note that our use of strain gradients also imposes limits on the amplitudes of the strains. For small strains, the nonlinear contributions, the largest of which are proportional to the square of strain, are necessarily small compared to the linear effect, which is proportional to strain. However, the contribution of the strain gradient is small as well. For the strain gradient term to dominate over the nonlinearities, the dimensionless ratio of lattice length scale $|\mathbf{l}_1|$ to the length scale of deformation, λ, while small, must nevertheless be large compared to the infinitesimal strain for our results to be quantitatively valid: $1 \gg |\mathbf{l}_1|/\lambda \gg \epsilon$.

VIII. CONCLUSIONS

We have presented a new method for describing the energetic effects of imposed macroscopic strain fields and their gradients on a microstructure that undergoes microscopic relaxation. We arrive at separate expressions for bulk and surface energies and establish, for critically coordinated systems, an elastic bulk-boundary correspondence between the bulk structure and topologically protected zero-energy modes. The underlying topological invariant establishes the relative numbers of zero modes on two opposing boundaries, as either number separately would rely on short-wavelength physics. This case establishes a sort of mesoscale elasticity, with topological surface modes existing on length scales far beyond the unit cell but necessarily far below the system size. Notably, this elasticity may lead to experimental demonstrations of topological polarization based on macroscale strains even when microscopic structure remains unobserved.

While we have used a periodic lattice to derive a periodic theory in order to connect with past work and demonstrate a simple connection between the lattice and continuum theories, nothing in the rigidity map of Eq. (18) requires an underlying lattice. The essential requirements for topological winding numbers are the mechanical criticality and the breaking of spatial inversion symmetry, which permit a well-defined, nontrivial topological state. Mechanical criticality can be achieved in large, nonlattice systems such as jammed packings [14,15] and biopolymer networks [17]. Jammed packings typically have spatial inversion symmetry, but it may be possible to break this by using particles that themselves lack this symmetry; certainly, it may be broken by coupling to external fields (such as substrate shape). In contrast, plausible candidates such as thin elastic sheets are not expected to support topological polarization since, while they are in some sense mechanically critical, they are the continuum limit of triangulated origami sheets, which were found not to polarize in Ref. [27].

These extensions of the lattice theory to the continuum present several avenues for further study. Lattice theories have considered bulk response [28], topological defects [25], buckling failure [26], and fracture [29]. All of these phenomena may extend to the continuum in intriguing ways. Following the realization of topological states in kirigami sheets [27], incorporating curvature into our continuum model may yield new physics. Examinations of finite-frequency topological modes, which have examined the continuum properties of the individual components [41,42], may be extended to wavelengths beyond that of the microstructure.

Intriguingly, recent work has also shown that topological boundary modes can arise even in amorphous systems due to the mesoscale structure [21]. Similarly, our surface theory relies on the short-length structure, suggesting that it may extend even to nonperiodic systems, though topological polarization still relies on breaking spatial inversion symmetry. If indeed such local structure can describe directional response, it may underlie artificial structures that program intricate mechanical responses [43–45], which are themselves inspired by biological allostery.

Nonlinearities, too, may prove tractable in the general continuum theory, such as when they lead to topologically protected solitons in one-dimensional systems [35] and to nonreciprocal mechanical response [46].

In the present work, which we encourage the reader to compare with the illuminating Ref. [47] (which was posted recently), we considered a critical balance between constraints and independent components of the strain field that was derived by the critical coordination of the microscopic system. It is an open question as to whether such theories may emerge in the continuum without being present in the microscopic system. Structures such as those consisting of rigid square pieces joined at corners have a nonlinear zero-energy dilation mode [4] and are well described by continuum theories [48,49]. However, such systems rely on symmetry to achieve their deformation mode and do not have zero-energy boundary modes.

ACKNOWLEDGMENTS

The authors gratefully acknowledge helpful conversations with Danilo Liarte and Jim Sethna. Part of this work was supported by the National Science Foundation through Grant No. NSF DMR-1308089 (D. Z. R.).

APPENDIX A: DERIVING THE EQUILIBRIUM MAP $Q_{ij,m}$ FROM THE RIGIDITY MAP $R_{m,ij}$

We expect the components of the stress tensor to be linear in the spring tensions e_m, and we define the equilibrium map as

$$\sigma_{ij}(\mathbf{r}) = Q_{ij,m} e_m(\mathbf{r}). \tag{A1}$$

The following analysis can be made on either prerelaxation or postrelaxation mappings. Given that the bonds' extensions are linear in the components of the strains,

$$e_m(\mathbf{r}) = R_{m,ij}\epsilon_{ij}(\mathbf{r}), \tag{A2}$$

the total energy of the system is

$$E = \frac{1}{2}\int d\mathbf{r} e_m^2(\mathbf{r}) = \frac{1}{2}\int d\mathbf{r}(R_{m,ij}\epsilon_{ij}(\mathbf{r}))^2. \tag{A3}$$

Given this result, we obtain

$$\sigma_{ij}(\mathbf{r}) = \frac{\delta E}{\delta \epsilon_{ij}(\mathbf{r})} \tag{A4a}$$

$$= \frac{\delta}{\delta \epsilon_{ij}(\mathbf{r})}\frac{1}{2}\int d\mathbf{r}(R_{m,ij}\epsilon_{ij}(\mathbf{r}))^2 \tag{A4b}$$

$$= R_{m,ij}R_{m,ij}\epsilon_{ij}(\mathbf{r}) \tag{A4c}$$

$$\Rightarrow \sigma_{ij}(\mathbf{r}) = R_{m,ij}e_m(\mathbf{r}), \tag{A4d}$$

where in the final line we used the linear relationship of Eq. (A2). From Eq. (A1), we recognize here the equilibrium mapping $Q_{ij,m}$, meaning

$$Q_{ij,m} = R_{m,ij}. \tag{A5}$$

We now consider how the stress field defined in Eq. (A1) relates to the conventional stress of Cauchy elasticity. In particular, what are the conditions on the stress field for equilibrium on the boundary and on the bulk? To find these conditions, we invoke the chain rule of functional derivatives, which we quickly rederive here. Consider a scalar function f that is a function of a vector with components $\{g_i\}$, each of which is a function of variables $\{x_j\}$. Then, with an implied sum over a repeated index,

$$\frac{\partial f}{\partial x_j} = \frac{\partial f}{\partial g_i}\frac{\partial g_i}{\partial x_j}. \tag{A6}$$

If we now treat the indices i, j as continuous (and vectorial) variables $\mathbf{r}, \mathbf{r}'$, then this becomes a functional relationship:

$$\frac{\delta f}{\delta x(\mathbf{r})} = \int d\mathbf{r}' \frac{\delta f}{\delta g(\mathbf{r}')}\frac{\delta g(\mathbf{r}')}{\delta x(\mathbf{r})}, \tag{A7}$$

where the sum over index i has become an integral over $\mathbf{r}'$ in the continuum limit. This result is relevant to the equilibrium problem because the energy functional is dependent on displacement only through the strains and their gradients. Furthermore, we can readily evaluate the functional derivative:

$$\frac{\delta \epsilon_{ij}(\mathbf{r}')}{\delta u_k(\mathbf{r})} = \frac{1}{2}(\delta_{jk}\partial_i + \delta_{ik}\partial_j)\delta(\mathbf{r}' - \mathbf{r}). \tag{A8}$$

We are now able to evaluate the force that the system exerts on material at $\mathbf{r}$ due to a particular displacement field:

$$f_k(\mathbf{r}) = -\frac{\delta E}{\delta u_k(\mathbf{r})} \tag{A9a}$$

$$= -\int d\mathbf{r}' \frac{\delta E}{\delta \epsilon_{ij}(\mathbf{r}')}\frac{\delta \epsilon_{ij}(\mathbf{r}')}{\delta u_k(\mathbf{r})} \tag{A9b}$$

$$= -(1/2)\int d\mathbf{r}'(\delta_{jk}\partial_i + \delta_{ik}\partial_j)\delta(\mathbf{r}' - \mathbf{r})\frac{\delta E}{\delta \epsilon_{ij}(\mathbf{r}')} \tag{A9c}$$

$$= (1/2)\left(\partial_i \frac{\delta E}{\delta \epsilon_{ik}(\mathbf{r})} + \partial_j \frac{\delta E}{\delta \epsilon_{kj}(\mathbf{r})}\right) \tag{A9d}$$

$$\Rightarrow f_k(\mathbf{r}) = \partial_i \frac{\delta E}{\delta \epsilon_{ik}(\mathbf{r})}. \tag{A9e}$$

Hence, we see that given our definition of stress as the functional derivative of the energy functional with respect to strain, we recover the standard bulk equilibrium condition that the stress tensor's gradient vanish: $\partial_i \sigma_{ij} = 0$.

What about the equations of equilibrium at the boundary? Let us suppose that there are no body forces and that forces are exerted only in a narrow range on the boundary. In particular, let us approximate forces as being applied over a boundary layer of infinitesimal thickness w. Then, by integrating the general equilibrium condition in the presence of spatially varying forces, $\partial_i \sigma_{ij} + f_j$, across the boundary, we acquire the usual condition on the stress in terms of the components n_i of the surface normal and the force per area on the boundary f_j^b:

$$n_i \sigma_{ij} = f_j^b. \tag{A10}$$

Additionally, we would then have, within the boundary layer itself,

$$\partial_i \sigma_{ij} = f_j^b / w. \tag{A11}$$

In this way, the force and the depth over which it is supplied may be used to impose boundary conditions on both the stress tensor and its first gradients.

APPENDIX B: RELATING EQUILIBRIUM AND RIGIDITY MAPS IN RECIPROCAL SPACE WITH PERIODIC STRUCTURE

In this section, we incorporate periodic structure into the relationships described in the previous section (Appendix A). As we will see, the dependence on the wave vector is reversed for the equilibrium and rigidity maps—the key result first obtained for lattice structures, which permits topological polarization. To that end, we first consider more general, nonlocal classes of rigidity and equilibrium maps than we have previously:

$$e_m(\mathbf{r}) = \int d\mathbf{r}' R_{m,ij}(\mathbf{r}, \mathbf{r}', \partial') \epsilon_{ij}(\mathbf{r}'), \tag{B1}$$

$$\sigma_{ij}(\mathbf{r}) = \int d\mathbf{r}' Q_{ij,m}(\mathbf{r}, \mathbf{r}', \partial') e_m(\mathbf{r}'), \tag{B2}$$

where the inclusion of "∂" indicates that the maps can involve gradients. Repeating the process above, we again obtain stresses from our energy functional. Now, though, we apply the well-known result that such functional differentiation flips the sign of the gradients. This case may be seen by explicitly writing out gradients of the delta functionals that are used in functional differentiation and integrating by parts. The result, in this case, is that

$$Q_{ij,m}(\mathbf{r}, \mathbf{r}', \partial') = \frac{\delta \sigma_{ij}(\mathbf{r})}{\delta e_m(\mathbf{r}')} \tag{B3a}$$

$$= \frac{\delta^2 E}{\delta \epsilon_{ij}(\mathbf{r}) \delta e_m(\mathbf{r}')}. \tag{B3b}$$

$$= \frac{\delta}{\delta \epsilon_{ij}(\mathbf{r})} \left(\frac{\delta E}{\delta e_m(\mathbf{r}')} \right) \tag{B3c}$$

$$= \frac{\delta}{\delta \epsilon_{ij}(\mathbf{r})} e_m(\mathbf{r}') \tag{B3d}$$

$$= \frac{\delta}{\delta \epsilon_{ij}(\mathbf{r})} \int d\mathbf{r}'' R_{m,ij}(\mathbf{r}', \mathbf{r}'', \partial'') \epsilon_{ij}(\mathbf{r}'') \tag{B3e}$$

$$= \int d\mathbf{r}'' R_{m,ij}(\mathbf{r}', \mathbf{r}'', \partial'') \delta(\mathbf{r}'' - \mathbf{r}), \tag{B3f}$$

leading to the desired result in real space:

$$Q_{ij,m}(\mathbf{r}, \mathbf{r}', \partial') = R_{m,ij}(\mathbf{r}', \mathbf{r}, -\partial). \tag{B4}$$

We now return to incorporating our system's translational invariance and (semi)local interactions, such that $R_{m,ij}(\mathbf{r}, \mathbf{r}', \partial) \to R_{m,ij}(\mathbf{r} - \mathbf{r}', \partial) \to \delta(\mathbf{r} - \mathbf{r}') R_{m,ij}(\partial)$. In reciprocal space, such that $\partial \to i\mathbf{q}$, we may then write the relationship between equilibrium and rigidity maps as

$$Q_{ij,m}(\mathbf{q}) = R_{m,ij}(-\mathbf{q}). \tag{B5}$$

Our linear relationships then have the form

$$e_m(\mathbf{q}) = R_{m,ij}(\mathbf{q}) \epsilon_{ij}(\mathbf{q}), \tag{B6}$$

$$\sigma_{ij}(\mathbf{q}) = Q_{ij,m}(\mathbf{q}) e_m(\mathbf{q}). \tag{B7}$$

APPENDIX C: ENERGY AND SURFACE TERMS

In this section, we find how the total energy of our system breaks down between surface and bulk terms, using the expression of our rigidity map,

$$E = \frac{1}{2} \sum_m \int d^d\mathbf{r} e_m(\mathbf{r}) e_m(\mathbf{r}), \tag{C1a}$$

$$e_m(\mathbf{r}) = \frac{b_i^m b_j^m}{|\mathbf{b}^m|} (1 + p_k^m \partial_k) \epsilon_{ij}(\mathbf{r}). \tag{C1b}$$

$$E = \frac{1}{2} \sum_m \int d^d\mathbf{r} \frac{b_i^m b_j^m b_k^m b_l^m}{|\mathbf{b}^m|^2} [(1 + p_\alpha^m \partial_\alpha) \epsilon_{ij}(\mathbf{r})] \times [(1 + p_\beta^m \partial_\beta) \epsilon_{kl}(\mathbf{r})] \tag{C2a}$$

$$= \frac{1}{2} \sum_m \frac{b_i^m b_j^m b_k^m b_l^m}{|\mathbf{b}^m|^2} \left(\int d^d\mathbf{r} [\epsilon_{ij}(\mathbf{r}) (\mathbf{p}_m \cdot \nabla) \epsilon_{kl}(\mathbf{r}) + \epsilon_{kl}(\mathbf{r}) (\mathbf{p}_m \cdot \nabla) \epsilon_{ij}(\mathbf{r})] + \int d^d\mathbf{r} [\epsilon_{ij}(\mathbf{r}) \epsilon_{kl}(\mathbf{r}) + (\mathbf{p}_m \cdot \nabla) \epsilon_{ij}(\mathbf{r}) (\mathbf{p}_m \cdot \nabla) \epsilon_{kl}(\mathbf{r})] \right). \tag{C2b}$$

The second term of Eq. (C2b) is a bulk term, and it cannot be simplified any further. However, the first term can be nicely expressed on the surface only using the divergence theorem:

$$E_s = \frac{1}{2} \sum_m \frac{b_i^m b_j^m b_k^m b_l^m}{|\mathbf{b}^m|^2} \mathbf{p}_m \cdot \left\{ \int d^d\mathbf{r} \nabla [\epsilon_{ij}(\mathbf{r}) \epsilon_{kl}(\mathbf{r})] \right\} \tag{C3a}$$

$$= \frac{1}{2}\sum_m \int_{\text{surface}} d^{d-1}\mathbf{r}(\mathbf{p}_m \cdot \hat{n}) \frac{b_i^m b_j^m b_k^m b_l^m}{|\mathbf{b}^m|^2} \epsilon_{ij}(\mathbf{r})\epsilon_{kl}(\mathbf{r}). \tag{C3b}$$

In Sec. III, we wrote the surface and bulk energies separately, and in terms of strains, their gradients, and the following elastic moduli:

$$A_{ijkl} = \sum_m \frac{b_i^m b_j^m b_k^m b_l^m}{|\mathbf{b}^m|^2}, \tag{C4a}$$

$$B^{\alpha}_{ijkl} = \sum_m \frac{b_i^m b_j^m b_k^m b_l^m}{|\mathbf{b}^m|^2} p_m^{\alpha}, \tag{C4b}$$

$$D^{\alpha\beta}_{ijkl} = \sum_m \frac{b_i^m b_j^m b_k^m b_l^m}{|\mathbf{b}^m|^2} p_m^{\alpha} p_m^{\beta}, \tag{C4c}$$

such that the total energy has the expression

$$E = E_s + E_b \tag{C5a}$$

$$= \frac{1}{2}\int_{\text{surface}} d^{d-1}\mathbf{r}\hat{n}_{\alpha} B^{\alpha}_{ijkl}\epsilon_{ij}\epsilon_{kl} + \frac{1}{2}\int d^d\mathbf{r} A_{ijkl}\epsilon_{ij}\epsilon_{kl} + D^{\alpha\beta}_{ijkl}(\partial_{\alpha}\epsilon_{ij})(\partial_{\beta}\epsilon_{kl}), \tag{C5b}$$

with the elastic moduli invariant under permutations of either their lower or their upper indices, as follows from their definitions in Eq. (C4).

Considering the system studied in Fig. 2, and given that our bonds and sites lie in the two-dimensional plane, the total number of different coefficients is reduced to the following:

(i,j,k,l)	A_{ijkl}	(B^x_{ijkl}, B^y_{ijkl})	$(D^{xx}_{ijkl}, D^{xy}_{ijkl}, D^{yy}_{ijkl})$
(x,x,x,x)	3.21878	(0.419412, −0.387303)	(0.358676, −0.0566132, 0.0893519)
(x,x,x,y)	−0.374777	(−0.167225, 0.0139916)	(0.110746, 0.00195441, 0.0193136)
(x,x,y,y)	0.621217	(−0.040412, −0.100059)	(0.216224, 0.0786884, 0.0891775)
(x,y,y,y)	0.274585	(−0.607169, −0.25146)	(0.312016, 0.377231, 0.178096)
(y,y,y,y)	2.94237	(−0.342389, −2.09884)	(2.14663, 0.16367, 1.63641)

The continuum theory described in Sec. V involves relaxation modes that alleviate unbalanced forces on microscopic elements. This process substantially complicates analytical expressions relating the gradient elasticity theory to the microstructure, but it does not qualitatively alter the phenomenology.

APPENDIX D: WINDING NUMBER

As described in the main text, the task of relating the number of modes on edges of the systems to their bulk systems reduces mathematically to counting the numbers of zeros in the complex plane. Here, we supply mathematical details and quantify the error associated with the long-wavelength approximation. This section implicitly uses a length scale so that we may treat physical quantities with units of length as pure numbers.

Physically, the points in the complex plane correspond to complex wave vectors. We draw a contour as shown in Fig. 3 of the main text, which encloses all zeros close to the origin [of order of the wave vector, which we term here $O(\epsilon)$] and avoids those far from the origin (of order 1). The latter are nonphysical since our theory only describes the long-wavelength limit. Because of the shape of the contour, zeros in the upper half-plane, corresponding to modes on the left edge, are enclosed in a positive orientation, while those in the lower half-plane are enclosed in a negative one. Note also that the contour in question allows a branch cut to be defined stretching along the negative real axis, which is important for evaluating the phase of complex numbers.

Were we to retain all components of the contour, the residue theorem would ensure that we could exactly evaluate the number of zeros enclosed by the contour (we choose a gauge in which no poles are present). However, in order to achieve bulk-boundary correspondence, we must identify the complex zeros by only considering the bulk modes, which lie on the real axis. We thus neglect the curved components of the contour. We now show that this approximation nevertheless recovers the result given in the main text, up to a small, controlled error.

Without loss of generality, we may consider the phase added to our contour integral from each zero separately. As such, we wish to obtain the change in phase of a complex function of the form

$$f(z) = z - z_0, \tag{D1}$$

as z winds along a contour $re^{i\theta}$, with θ going from 0 to either π or $-\pi$. Here, we choose r to be much larger than long-wavelength zeros $[O(\epsilon^1)]$ but much smaller than the short-wavelength ones $[O(\epsilon^0)]$.

Because the argument of the complex number is simply the imaginary part of its logarithm, we immediately obtain two results. First, the contribution of the straight sections of the contour, which we retain, is the expression given in the main text. Second, the contribution from the curved parts that we neglect is

$$2\mathrm{Im}\log\left|\frac{r+z_0}{r-z_0}\right|. \tag{D2}$$

Note here that although the long-wavelength zeros have a real part $O(\epsilon^1)$ they also have an imaginary part $O(\epsilon^2)$; hence, we find that for $|r| \gg |z_0|$, the error is of order $O(\epsilon^2/r)$. In contrast, the error from the short-wavelength, spurious modes is of order $O(r)$, assuming that our original contour actually encloses all of the long-wavelength zero modes. However, if this condition is not met, the error in the calculation of the change in phase increases abruptly to $O(1)$. To minimize the error, we should then select the bounds of our contour to minimize their size while ensuring that they capture the essential physics. In the main text, we make the natural choice for r to lie intermediate between the two regimes—$r = \epsilon^{1/2}$ in units in which unit cell size is of order one, generating error of $O(\epsilon^{1/2})$. More aggressive schemes, such as $r = \epsilon^{3/4}, \epsilon^{0.99}$, could more closely characterize the topological transition but would require greater knowledge of the microscopic details or willingness to tolerate occasional large errors.

As discussed above, the error from the true determinant function may be obtained simply by summing over a few cases of these zeros and is thus of the same order. Thus, we have shown, using complex analysis, that in the long-wavelength limit, the correspondence between the bulk structure and the imbalance of topological edge modes given in Eq. (20) of the main text,

$$N_L - N_R = \frac{1}{\pi}\lim_{\epsilon\to 0^+}\int_{-\sqrt{\epsilon}/|\mathbf{l}_1|}^{\sqrt{\epsilon}/|\mathbf{l}_1|} dq_x \partial_{q_x} \arg\det\left(\mathbf{R}(q_x, q_y = \epsilon)\right), \tag{D3}$$

is mathematically justified. We emphasize here that this is not because the bulk modes along the curved parts of the contour are negligible but because the choice of contour causes them to cancel out. Thus, bulk-boundary correspondence in the long-wavelength limit links together two boundaries at once, in contrast to the lattice theory.

APPENDIX E: SOFT DIRECTIONS, LENGTH SCALES, AND CHOICE OF MATHEMATICAL BASIS

In the main text, we introduce a number of different bases for the wave vectors. First, we have a simple Cartesian basis $(\hat{q}_x, \hat{q}_y)$. Second, we present a rotated version thereof, in order to accommodate boundaries with varying orientations, in terms of the inward-facing normal direction $\hat{q}_n$ and the tangent direction $\hat{q}_t$. Finally, we consider the two soft directions, along which there lie modes that satisfy the structural constraints to linear order, pointing along (nonorthogonal directions) $(\hat{q}_+, \hat{q}_-)$. We use the symbols $\alpha_\pm$, $\alpha_\pm(\theta_n)$ to relate these:

$$\begin{aligned}\hat{q}_\pm &= \frac{1}{\sqrt{1+\alpha_\pm^2}}(\alpha_\pm \hat{q}_x + \hat{q}_y) \\ &= \frac{1}{\sqrt{1+\alpha_+^2(\theta_n)}}(\alpha_+(\theta_n)\hat{q}_n + \hat{q}_t).\end{aligned} \tag{E1}$$

As discussed in the main text, the bulk structure requires that zero modes occur at wave vectors satisfying the following constraint:

$$q_x = \alpha_\pm q_y + i\beta \pm q_y^2. \tag{E2}$$

We now consider a boundary mode that has the component q_t along the tangent direction and thus takes the form $q_n\hat{q}_n + q_t\hat{q}_t$. By requiring that this mode satisfies the above constraints to *second* order, we obtain a result for the coefficients $\alpha_\pm(\theta_n)$, which define the soft directions:

$$q_n = \alpha_\pm(\theta_n)q_t + i\beta_\pm(\theta_n)q_t^2. \tag{E3}$$

In the $\hat{q}_n, \hat{q}_t$ basis, we know the expression of $\mathbf{q}$. Let us assume that $\mathbf{q}$ is a zero of our map; therefore, it has the following form:

$$\mathbf{q} = q_t(\alpha_+(\theta_n)\hat{q}_n + \hat{q}_t) + i\kappa_+(\theta_n)q_t^2\hat{q}_n. \tag{E4}$$

We recognize that the leading-order contribution to this zero-energy edge mode is simply the bulk soft mode. Expressing it in this form explicitly, we may write

$$\mathbf{q} = \frac{q_t}{\hat{q}_+\cdot\hat{q}_t}\hat{q}_+ + i\kappa_+(\theta_n)q_t^2\hat{q}_n, \tag{E5a}$$

$$\mathbf{q} = q_+\hat{q}_+ + i\kappa_+(\theta_n)(\hat{q}_+\cdot\hat{q}_t)^2 q_+^2\hat{q}_n, \tag{E5b}$$

where q_+ represents the value of the mode along the soft direction, while q_t is the value of the mode along the transverse direction of the normal. Now, consider such a mode that, say, lies to first order along the $\hat{q}_+$ direction. For it to be a zero mode, it must contain a second-order correction along the $\hat{q}_-$ direction that satisfies the zero-energy condition, which in this basis has a simplified expression:

$$\begin{aligned}\det\left(\mathbf{R}(\mathbf{q})\right) =& A''_{1,1}q_+q_- + i(A''_{3,0}q_+^3 + A''_{2,1}q_+^2q_- \\ &+ A''_{1,2}q_-q_+^2 + A''_{0,3}q_-^3) = 0.\end{aligned} \tag{E6}$$

The term $\hat{q}_n$ may be decomposed into contributions in the $\hat{q}_\pm$ directions, leading to an $O(q_+^2)$ contribution to q_- from the wave vector of Eq. (E5b). This result means that

the $O(q_+^2)$ term of the determinant of Eq. (E6) vanishes automatically. Requiring that the next leading term vanish as well allows us to derive the leading decay factor in a zero mode:

$$\mathbf{q} = \frac{q_t}{\sin(\theta_+ - \theta_n)}\hat{q}_+ + iq_t^2 \frac{A''_{3,0}}{A''_{1,1}} \frac{\sin(\theta_+ - \theta_-)}{\sin^3(\theta_n - \theta_+)}\hat{q}_n, \tag{E7a}$$

$$\mathbf{q} = q_+\hat{q}_+ + iq_+^2 \frac{A''_{3,0}}{A''_{1,1}} \frac{\sin(\theta_+ - \theta_-)}{\sin(\theta_n - \theta_+)}\hat{q}_n. \tag{E7b}$$

Finally, as we explain in the main text, we find that some of the system's parameters are dependent of the size of the cell $|\mathbf{l}_1|$, particularly that the quantity $A''_{3,0}/(A''_{1,1}|\mathbf{l}_1|)$ is dimensionless. In addition to expressing the wave vector q_t in terms of its wavelength λ ($q_t = 2\pi/\lambda$), we can then derive an expression for a zero mode as a function of the properties on the boundary and the associated decay length through the bulk ζ_+:

$$\mathbf{q} = \frac{2\pi}{\lambda \sin(\theta_+ - \theta_n)}\hat{q}_+ + i\left(\frac{2\pi}{\lambda}\right)^2 \frac{A''_{3,0}}{A''_{1,1}} \frac{\sin(\theta_+ - \theta_-)}{\sin^3(\theta_n - \theta_+)}\hat{q}_n \tag{E8}$$

$$\Rightarrow \left[\frac{\zeta_+}{|\mathbf{l}_1|}\right] = \left[\frac{\lambda}{2\pi|\mathbf{l}_1|}\right]^2 \left[\frac{|\mathbf{l}_1|A''_{1,1}}{A''_{3,0}}\right] \frac{\sin^3(\theta_n - \theta_+)}{\sin(\theta_+ - \theta_-)}. \tag{E9}$$

[1] G. W. Milton and A. V. Cherkaev, *Which Elasticity Tensors Are Realizable?*, J. Eng. Mater. Technol. **117**, 483 (1995).

[2] M. Kadic, T. Bückmann, N. Stenger, M. Thiel, and M. Wegener, *On the Practicability of Pentamode Mechanical Metamaterials*, Appl. Phys. Lett. **100**, 191901 (2012).

[3] C. P. Goodrich, A. J. Liu, and S. R. Nagel, *The Principle of Independent Bond-Level Response: Tuning by Pruning to Exploit Disorder for Global Behavior*, Phys. Rev. Lett. **114**, 225501 (2015).

[4] J. N. Grima and K. E. Evans, *Auxetic Behavior from Rotating Squares*, J. Mater. Sci. Lett. **19**, 1563 (2000).

[5] W. Yang, Z.-M. Li, W. Shi, B.-H. Xie, and M.-B. Yang, *Review on Auxetic Materials*, J. Mater. Sci. **39**, 3269 (2004).

[6] A. Alderson and K. L. Alderson, *Auxetic Materials*, P I Mech Eng G-J Aer **221**, 565 (2007).

[7] M. Hanifpour, C. F. Petersen, M. J. Alava, and S. Zapperi, *Mechanics of Disordered Auxetic Metamaterials*, Eur. Phys. J. B **91**, 271 (2018).

[8] K. Bertoldi, V. Vitelli, J. Christensen, and M. van Hecke, *Flexible Mechanical Metamaterials*, Nat. Rev. Mater. **2**, 17066 (2017).

[9] M. K. Blees, A. W. Barnard, P. A. Rose, S. P. Roberts, K. L. McGill, P. Y. Huang, A. R. Ruyack, J. W. Kevek, B. Kobrin, D. A. Muller *et al.*, *Graphene Kirigami*, Nature (London) **524**, 204 (2015).

[10] Q. Chen, S. C. Bae, and S. Granick, *Directed Self-Assembly of a Colloidal Kagome Lattice*, Nature (London) **469**, 381 (2011).

[11] J. Cha, K. W. Kim, and C. Daraio, *Experimental Realization of On-Chip Topological Nanoelectromechanical Metamaterials*, Nature (London) **564**, 229 (2018).

[12] P. W. K. Rothemund, *Folding DNA to Create Nanoscale Shapes and Patterns*, Nature (London) **440**, 297 (2006).

[13] C. E. Castro, F. Kilchherr, D.-N. Kim, E. L. Shiao, T. Wauer, P. Wortmann, M. Bathe, and H. Dietz, *A Primer to Scaffolded DNA Origami*, Nat. Methods **8**, 221 (2011).

[14] A. J. Liu and S. R. Nagel, *Nonlinear Dynamics: Jamming Is Not Just Cool Any More*, Nature (London) **396**, 21 (1998).

[15] S. Torquato, A. Donev, and F. H. Stillinger, *Breakdown of Elasticity Theory for Jammed Hard-Particle Packings: Conical Nonlinear Constitutive Theory*, Int. J. Solids Struct. **40**, 7143 (2003).

[16] D. J. Jacobs and M. F. Thorpe, *Generic Rigidity Percolation: The Pebble Game*, Phys. Rev. Lett. **75**, 4051 (1995).

[17] C. P. Broedersz and F. C. MacKintosh, *Modeling Semiflexible Polymer Networks*, Rev. Mod. Phys. **86**, 995 (2014).

[18] A. C. Eringen, *Mechanics of Micromorphic Continua*, in *Mechanics of Generalized Continua* (Springer, New York, 1968), pp. 18–35.

[19] D. Zhou, L. Zhang, and X. Mao, *Topological Boundary Floppy Modes in Quasicrystals*, Phys. Rev. X **9**, 021054 (2019).

[20] D. Varjas, A. Lau, K. Pöyhönen, A. R. Akhmerov, D. I. Pikulin, and I. C. Fulga, *Topological Phases without Crystalline Counterparts*, Phys. Rev. Lett. **123**, 196401 (2019).

[21] N. P. Mitchell, L. M. Nash, D. Hexner, A. M. Turner, and W. T. M. Irvine, *Amorphous Topological Insulators Constructed from Random Point Sets*, Nat. Phys. **14**, 380 (2018).

[22] D. Bartolo and D. Carpentier, *Topological Elasticity of Nonorientable Ribbons*, Phys. Rev. X **9**, 041058 (2019).

[23] C. L. Kane and T. C. Lubensky, *Topological Boundary Modes in Isostatic Lattices*, Nat. Phys. **10**, 39 (2014).

[24] X. Mao and T. C. Lubensky, *Maxwell Lattices and Topological Mechanics*, Annu. Rev. Condens. Matter Phys. **9**, 413 (2018).

[25] J. Paulose, B. G.-g. Chen, and V. Vitelli, *Topological Modes Bound to Dislocations in Mechanical Metamaterials*, Nat. Phys. **11**, 153 (2015).

[26] J. Paulose, A. S. Meeussen, and V. Vitelli, *Selective Buckling via States of Self-Stress in Topological Metamaterials*, Proc. Natl. Acad. Sci. U.S.A. **112**, 7639 (2015).

[27] B. G.-g. Chen, B. Liu, A. A. Evans, J. Paulose, I. Cohen, V. Vitelli, and C. D. Santangelo, *Topological Mechanics of Origami and Kirigami*, Phys. Rev. Lett. **116**, 135501 (2016).

[28] D. Z. Rocklin, *Directional Mechanical Response in the Bulk of Topological Metamaterials*, New J. Phys. **19**, 065004 (2017).

[29] L. Zhang and X. Mao, *Fracturing of Topological Maxwell Lattices*, New J. Phys. **20**, 063034 (2018).

[30] T. C. Lubensky, C. L. Kane, X. Mao, A. Souslov, and K. Sun, *Phonons and Elasticity in Critically Coordinated Lattices*, Rep. Prog. Phys. **78**, 073901 (2015).

[31] C. R. Calladine, *Buckminster Fuller's Tensegrity Structures and Clerk Maxwell's Rules for the Construction of Stiff Frames*, Int. J. Solids Struct. **14**, 161 (1978).

[32] S. Meiboom, J. P. Sethna, P. W. Anderson, and W. F. Brinkman, *Theory of the Blue Phase of Cholesteric Liquid Crystals*, Phys. Rev. Lett. **46**, 1216 (1981).
[33] S. D. Guest and J. W. Hutchinson, *On the Determinacy of Repetitive Structures*, J. Mech. Phys. Solids **51**, 383 (2003).
[34] D. Z. Rocklin, S. Zhou, K. Sun, and X. Mao, *Transformable Topological Mechanical Metamaterials*, Nat. Commun. **8**, 14201 (2017).
[35] B. G.-g. Chen, N. Upadhyaya, and V. Vitelli, *Nonlinear Conduction via Solitons in a Topological Mechanical Insulator*, Proc. Natl. Acad. Sci. U.S.A. **111**, 13004 (2014).
[36] M. Baus and R. Lovett, *Generalization of the Stress Tensor to Nonuniform Fluids and Solids and Its Relation to Saint-Venant's Strain Compatibility Conditions*, Phys. Rev. Lett. **65**, 1781 (1990).
[37] S. Shankar, M. J. Bowick, and M. C. Marchetti, *Topological Sound and Flocking on Curved Surfaces*, Phys. Rev. X **7**, 031039 (2017).
[38] A. Souslov, B. C. Van Zuiden, D. Bartolo, and V. Vitelli, *Topological Sound in Active-Liquid Metamaterials*, Nat. Phys. **13**, 1091 (2017).
[39] D. Z. Rocklin, B. G.-g. Chen, M. Falk, V. Vitelli, and T. C. Lubensky, *Mechanical Weyl Modes in Topological Maxwell Lattices*, Phys. Rev. Lett. **116**, 135503 (2016).
[40] O. R. Bilal, R. Süsstrunk, C. Daraio, and S. D. Huber, *Intrinsically Polar Elastic Metamaterials*, Adv. Mater. **29**, 1700540 (2017).
[41] J. Ma, D. Zhou, K. Sun, X. Mao, and S. Gonella, *Edge Modes and Asymmetric Wave Transport in Topological Lattices: Experimental Characterization at Finite Frequencies*, Phys. Rev. Lett. **121**, 094301 (2018).
[42] M. Miniaci, R. K. Pal, B. Morvan, and M. Ruzzene, *Experimental Observation of Topologically Protected Helical Edge Modes in Patterned Elastic Plates*, Phys. Rev. X **8**, 031074 (2018).
[43] J. W. Rocks, N. Pashine, I. Bischofberger, C. P. Goodrich, A. J. Liu, and S. R. Nagel, *Designing Allostery-Inspired Response in Mechanical Networks*, Proc. Natl. Acad. Sci. U.S.A. **114**, 2520 (2017).
[44] L. Yan, R. Ravasio, C. Brito, and M. Wyart, *Architecture and Coevolution of Allosteric Materials*, Proc. Natl. Acad. Sci. U.S.A. **114**, 2526 (2017).
[45] J. Z. Kim, Z. Lu, S. H. Strogatz, and D. S. Bassett, *Conformational Control of Mechanical Networks*, Nat. Phys. **15**, 714 (2019).
[46] C. Coulais, D. Sounas, and A. Alù, *Static Non-reciprocity in Mechanical Metamaterials*, Nature (London) **542**, 461 (2017).
[47] K. Sun and X. Mao, *Universal Continuum Theory for Topological Edge Soft Modes*, arXiv:1907.13163.
[48] C. Coulais, C. Kettenis, and M. van Hecke, *A Characteristic Length Scale Causes Anomalous Size Effects and Boundary Programmability in Mechanical Metamaterials*, Nat. Phys. **14**, 40 (2018).
[49] B. Deng, C. Mo, V. Tournat, K. Bertoldi, and J. R. Raney, *Focusing and Mode Separation of Elastic Vector Solitons in a 2D Soft Mechanical Metamaterial*, Phys. Rev. Lett. **123**, 024101 (2019).